Short communication

Direct methanol fuel cell bubble transport simulations via thermal lattice Boltzmann and volume of fluid methods

K. Fei, T.S. Chen, C.W. Hong *

Department of Power Mechanical Engineering, National Tsing Hua University, 101, Sec. 2, Kwang Fu Road, Hsinchu 30013, Taiwan

ABSTRACT

Carbon dioxide bubble removal at the anode of a direct methanol fuel cell (DMFC) is an important technique especially for applications in the portable power sources. This paper presents numerical investigations of the two-phase flow, CO_2 bubbles in a liquid methanol solution, in the anode microchannels from the aspect of microfluidics using a thermal lattice Boltzmann model (TLBM). The main purpose is to derive an efficient and effective computational scheme to deal with this technical problem. It is then examined by a commercially available software using Navier–Stokes plus volume of fluid (VOF) method. The latter approach is normally employed by most researchers. A simplified microchannel simulation domain with the dimension of $1.5\,\mu m$ in height (or width) and $16.0\,\mu m$ in length has been setup for both cases to mimic the actual flow path of a CO_2 bubble inside an anodic diffusion layer in the DMFC. This paper compares both numerical schemes and results under the same operation conditions from the viewpoint of fuel cell engineering.

© 2009 Elsevier B.V. All rights reserved.

1. Introduction

Transport dynamics of carbon dioxide (CO_2) bubbles in microchannels have drawn much attention in recent years. It is an important issue at the anode of a direct methanol fuel cell (DMFC), which is a potential electric generator for future portable electronic products. Without efficient removal of CO_2 bubbles at the anode, the flow channel and the porous diffusion layer of the DMFC will be blocked. Thus the anodic reactant, i.e. the methanol–water solution, cannot evenly distribute to the catalyst site, resulting in a decline of the DMFC performance, possibly causing failure of operation. To investigate the CO_2 bubble dynamics, Lu and Wang [1] employed a digital video camera to visualize the bubble flow in the anode and water flooding in the cathode. In situ visualization of CO_2 bubble behavior in anode flow fields was also conducted by Yang et al. [2] and Wong et al. [3]. The experimental technique is practicable to give us insight into the bubble behavior in flow channels which are in mm scale. However, the bubbles are released uncontrollably and it is a challenge to observe the detailed bubble behavior experimentally inside the non-transparent diffusion layers, which are in μm scale. Therefore, microfluidic analysis and flow animation are excellent research tools to perform the investigation of the bubble dynamics in such a micro-scale environment. Our lab has spent past 3 years to develop such a simulation tool [4,5].

The current progress focuses on the thermal effect, which is an important factor that significantly affects the bubble movement in a microchannel. This is because the contact force between the gas, liquid and the solid wall is mainly a function of temperature. The difference in the surface tension leads to a tangential force at the gas–liquid interface, and the direction of the tangential force is opposite to the temperature gradient. The liquid around the bubble surface flows from the hot area to the cold region due to the action of the tangential force. The motion of the liquid around the bubble surface provides a reacting force, making the bubble transport from the cold to the hot direction. The phenomenon of the bubble movement due to the temperature gradient, also known as the Marangoni effect, was firstly observed by Young et al. [6] through experiments. The concept of using the temperature gradient as a driving force of the bubble movement had been employed in microfluidic devices [7–9]. In the present work, we intend to apply this concept to the technique of the CO_2 bubble removal at the anode of the DMFC.

Several researches are involved in the development of the thermal lattice Boltzmann model for a single-phase flow [10–12]. Fei et al. [13] established a two-phase thermal lattice Boltzmann model, which is capable of simulating the dynamic temperature distribution of a bubble flow. Based on this work, we further discuss the details of the thermal effect on the CO_2 bubble transport phenomena in this research. The results obtained from the thermal lattice Boltzmann model are verified by a two-phase flow simulation using the volume of fluid (VOF) method, which is a popular technique in continuum fluid mechanics for simulat-

* Corresponding author. Tel.: +886 3 5742591; fax: +886 3 5722840.
E-mail address: cwhong@pme.nthu.edu.tw (C.W. Hong).

Nomenclature

Nomenclature

$\mathbf{e}$	lattice velocity vector
e	lattice speed (cm s^{-1})
f	density distribution function
g	thermal distribution function
$G^{\sigma\sigma'}$	interaction strength between the species σ and the other species σ' (cm^3 g^{-1} s^{-1})
G^{σ}	fluid–solid interaction potential parameter of the species σ
$\mathbf{G}$	gravitational constant (cm s^{-2})
G'	non-dimensional constant
m	material property
T	temperature (K)
t	time (s)
$\mathbf{U}$	velocity vector (u, v)
u	velocity in the x-direction (cm s^{-1})
v	velocity in the y-direction (cm s^{-1})
$\mathbf{X}$	position vector (x, y)

Greek symbols

α	volume fraction
β	thermal expansion coefficient (K^{-1})
κ	surface tension coefficient (N m^{-1})
ρ	density (g cm^{-3})
τ	collision time for momentum transfer
τ_T	collision time for heat transfer
ψ	function of the mass density

Subscript

i	lattice velocity directions
j	jth species
k	kth species
∞	reference state

Superscript

eq	equilibrium state
σ	species

ing multi-phase flows [14–16]. Both methods are described as below.

2. Numerical methods

2.1. Thermal lattice Boltzmann method (TLBM)

The Boltzmann equation was originally derived from Newton's laws at the low-density limit, without the assumption of the continuum. Here we assume that the microfluidic dynamics and thermal gas dynamics in the entire Knudsen region is governed by this equation, which is described by the evolution of a velocity distribution function, $f(x, t)$, by molecular transport and binary intermolecular collisions. The thermal lattice Boltzmann model used in our present research, including the derivation of the boundary conditions, has been described in detail in our previous work [13]. Only important solving procedures are described as below. The general form for the thermal lattice Boltzmann method to solve the momentum and energy transfer can be expressed as,

$$f_i(\mathbf{X} + \mathbf{e}_i \; \Delta t, t + \Delta t) - f_i(\mathbf{X}, t) = -\frac{1}{\tau} \cdot [f_i(\mathbf{X}, t) - f_i^{(eq)}(\mathbf{X}, t)] \tag{1}$$

$$g_i(\mathbf{X} + \mathbf{e}_i \; \Delta t, t + \Delta t) - g_i(\mathbf{X}, t) = -\frac{1}{\tau_T} \cdot [g_i(\mathbf{X}, t) - g_i^{(eq)}(\mathbf{X}, t)] \tag{2}$$
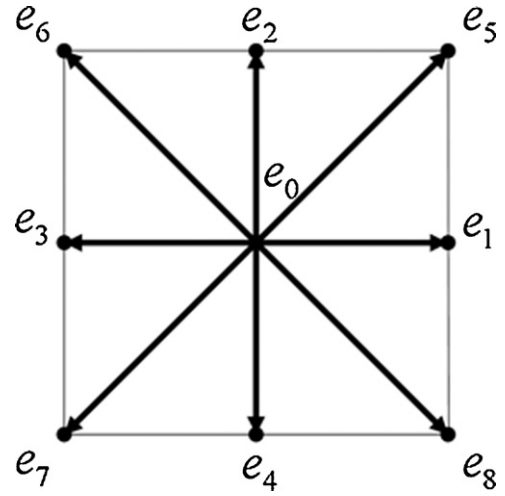

Fig. 1. The basic lattice of the D2Q9 model with the velocity vector defined in each direction (denoted by 0 to 8).

where $f_i(\mathbf{X}, t)$ and $g_i(\mathbf{X}, t)$ are the velocity distribution function and the thermal distribution function, respectively. They are both functions of space $\mathbf{X}$ and time t. Notation $\mathbf{e}_i$ represents the lattice velocity vector in the i direction; Greek symbol τ is the dimensionless collision time for momentum transfer while τ_T is the dimensionless collision time for energy transfer. The superscript eq stands for the equilibrium state. Although a three-dimensional approach can be easily derived, only two-dimensional, nine-velocity (D2Q9) model was adopted in this paper for fundamental research. The basic lattice of the D2Q9 model with each velocity defined in each direction is illustrated in Fig. 1.

The mathematical form of the equilibrium thermal distribution function, $g_i^{(eq)}(\mathbf{X}, t)$, for the D2Q9 model had been rigorously derived by Shi et al. [11]. It is expressible as

$$g_i^{(eq)} = w_i \rho T \left[1 + 3\frac{\mathbf{e}_i \cdot \mathbf{U}}{e^2} + \frac{9}{2}\frac{(\mathbf{e}_i \cdot \mathbf{U})^2}{e^4} - \frac{3}{2}\frac{(\mathbf{U} \cdot \mathbf{U})}{e^2} \right] \tag{3}$$

in which ρ is the density of the flow field at the specific position; $\mathbf{U}$ is the velocity vector, which includes velocities u in the x-direction and v in the y-direction. For the D2Q9 model, w_i equals to 4/9, 1/9 and 1/36 for $i = 0$, $i = 1$–4 and $i = 5$–8, respectively. The temperature field, $T(\mathbf{X}, t)$, is calculated from the equation of the thermal energy density,

$$\rho^{\sigma}(\mathbf{X}, t)T^{\sigma}(\mathbf{X}, t) = \sum_i g_i^{\sigma}(\mathbf{X}, t) \tag{4}$$

in which the superscript σ indicates different species. The equation states that the temperature of the species σ in the flow field is the quotient of the sum over the thermal distribution functions divided by the mass density, $\rho^{\sigma}(\mathbf{X}, t)$.

The basic scheme for solving the thermal lattice Boltzmann model in this research is to treat the additional effect of the thermal bubble flow as source terms to the momentum equation, which is expressed by

$$\rho^{\sigma}(\mathbf{X}, t)\mathbf{U}^{\sigma}(\mathbf{X}, t) = \sum_i f_i^{\sigma}(\mathbf{X}, t)\mathbf{e}_i + F_{\text{total}}^{\sigma}(\mathbf{X}, t) \tag{5}$$

In the above equation, the source term with the subscript total, $F_{\text{total}}^{\sigma}(\mathbf{X}, t)$, includes all the effects from the surface tension, the fluid–solid wall interaction, the buoyancy force, and the thermal effect. They are listed as below:

$$F_{\text{surface tension}}^{\sigma}(\mathbf{X}, t) = -\tau^{\sigma}[\psi^{\sigma}(\mathbf{X}, t)\sum_{\sigma'} G^{\sigma\sigma'}\sum_i \psi^{\sigma'}(\mathbf{X} + \mathbf{e}_i \Delta t, t)\mathbf{e}_i] \tag{6}$$

$$F_{solid}^{\sigma}(\mathbf{X}, t) = -\rho^{\sigma}(\mathbf{X}, t)\sum_i G_i^{\sigma}s(\mathbf{X} + \mathbf{e}_i \ \Delta t)\mathbf{e}_i \tag{7}$$

$$F_{buoyancy}^{\sigma}(\mathbf{X}, t) = g\sum_i \rho^{\sigma}(\mathbf{X} + \mathbf{e}_i \ \Delta t, t)\mathbf{e}_i \tag{8}$$

$$F_{thermal}^{\sigma}(\mathbf{X}, t) = \rho_{\infty}^{\sigma}(\mathbf{X}, t)\beta^{\sigma}\mathbf{G}(T^{\sigma} - T_{\infty}^{\sigma}) \tag{9}$$

where $\psi^{\sigma}(\mathbf{X}, t)$ is a function of the mass density of species σ; $G^{\sigma\sigma'}$ denotes the interaction strength between different species and is simplified to be a constant; G^{σ} is a parameter of the fluid–solid interaction potential; s is a function of the particle position ($s = 0$ when the particle is in the fluid, $s = 1$ when the particle is at the fluid/solid interface); G' is a non-dimensional constant; $\beta\sigma$ is the thermal expansion coefficient of species σ; $\mathbf{G}$ is the gravitational constant; ρ_{∞} and T_{∞} are the reference density and temperature, respectively. From the physical viewpoint, the thermal effect (Eq. (9)) is an additional force generated from the density variation which is caused by the temperature gradient in the flow field. This thermal effect becomes significant when the system scale is reduced to the micro-scale, such as the microchannel flow in our case.

2.2. Volume of fluid (VOF) method

The volume of fluid (VOF) method was originally proposed by Hirt and Nichols in the early 1980s [17]. It has been widely embedded in general commercial codes to solve problems regarding multi-phase and immiscible fluids. We used the commercial software, ADINA 8.4 [18], by choosing the VOF method, to examine our simulation results generated from the TLBM described above. The purpose is to verify the accuracy and efficiency of the TLBM method at this stage, although a microfluidic experiment under the same operation condition is still necessary for final assurance in the future.

The VOF method treats different fluid species in the multi-phase immiscible flow with the same transport equation using the conventional finite volume approach. Tracking of the interface boundary between multi-phases is accomplished by computing a volume fraction, α_j, from the volume fraction equation similar to the continuity equation,

$$\frac{\partial}{\partial t}\alpha_j + \mathbf{U} \cdot \nabla\alpha_j = 0, \quad j = 1, \ldots, n \tag{10}$$

in which subscript j stands for the jth species; n is the total number of the additional species beside the primary fluid. The value of α_j in each computational grid is from 0 to 1; $\alpha_j = 1$ stands for the grid is totally occupied by the jth species, $\alpha_j = 0$ means that the jth species does not exist in this computational grid. Any value of α_j between 0 and 1 means that the computational grid is a mixed volume, which is partially occupied by the jth species and the rest by the others. A material property m in the mixed grid is calculated as an average among all species,

$$m = \sum_{j=0}^{n}\alpha_j m_j \tag{11}$$

Note that the volume fraction of the primary fluid, α_0, is calculated by

$$\alpha_0 = 1 - \sum_{j=1}^{n}\alpha_j \tag{12}$$

In addition, a piecewise linear interface calculation (PLIC) method proposed by Youngs [19] is employed to reconstruct the interface between different species.
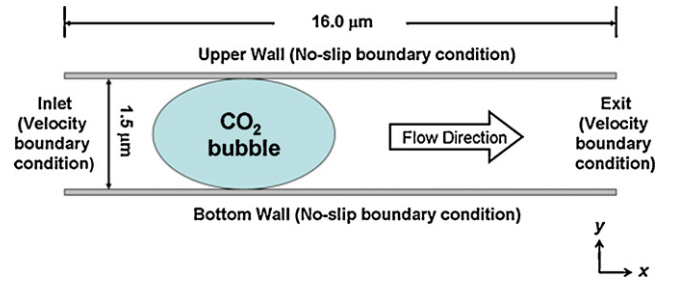

Fig. 2. Schematic diagram of the simulation domain of the bubbly thermal flow in a microchannel in which x-axis is the flow direction and y-axis is opposite to the gravity. The microchannel is 16.0 μm long and 1.5 μm high. No-slip boundary conditions are applied at the upper and bottom walls, while velocity boundary conditions are imposed at the inlet and exit of the microchannel.

A continuum surface force (CSF) model [20] is coupled with the VOF method in ADINA 8.4 to compute the surface tension of the two-phase (gas–liquid) flow. The CSF model considers the surface tension force, f_{st}, as a body force to the momentum equation. It is evaluated per unit volume and is expressed by

$$f_{st} = \sum_{j=0}^{n-1}\sum_{k=j+1}^{n}\kappa_{jk}(\alpha_j\Gamma_k\nabla\alpha_k + \alpha_k\Gamma_j\nabla\alpha_j) \tag{13}$$

in which κ_{jk} is the surface tension coefficient between jth and kth species; Γ_j is the curvature at the liquid–gas interface and is computed from

$$\Gamma_j = -\nabla \cdot \left(\frac{\nabla\alpha_j}{|\nabla\alpha_j|}\right) \tag{14}$$

3. Results and discussion

In this paper, we set up a straight microchannel to be the simulation domain. The microchannel mimics one of many actual flow paths of the CO_2 inside the porous diffusion/catalyst layers in a DMFC. Fig. 2 is the schematic diagram of the microchannel, which is 1.5 μm high and 16.0 μm long. The dimension of the simulation domain was chosen as the same order as the real flow path. The abscissa is assigned to be the same direction of the main flow (methanol–water solution), while the y-axis is opposite to the gravity. A single bubble is initially generated at the left-hand side of the microchannel in all simulation cases. The upper and the bottom walls are assumed to be no-slip. Inflow and outflow boundary conditions are assigned to the inlet and exit of the simulation domain. In order to focus on the investigation of thermal effects on the bubble transport phenomena, we conduct thermal lattice Boltzmann simulations with varied wall temperatures. Also all the simulation cases are conducted again using the VOF method to verify our TLBM scheme.

3.1. Bubble transport phenomena in the microchannel

The baseline TLBM simulation sets the temperature of both upper and bottom walls at 308 K and the inflow velocity of the methanol–water solution is fixed at 250 μm s^{-1} (pushed by a micro-pump). All the major input parameters of this base case are listed in Table 1. The computational grids used in this TLBM simulation are 0.05 μm × 0.05 μm rectangular cells; there are 9540 computational grids in total. Fig. 3 shows the TLBM simulation results. In Fig. 3(a) the density plot indicates that the contact angle remains the same (18.0°) along the flow path. The bubble is constrained by the dimension of the microchannel and becomes a bubble slug. The inflow velocity of the methanol–water solution

Table 1
Flow conditions and major input parameters in the TLBM simulation of the baseline case.

Microchannel specification and flow condition	
Channel length (μm)	16.0
Channel height (μm)	1.5
Wall temperature (K)	308
Inflow velocity (μm s^{-1})	250
Input parameters	
Interaction strength between species $G^{\sigma\sigma'}$ (cm^3 g^{-1} s^{-1})	3.78
Fluid–solid interaction potential G^{σ}	−0.004
Thermal expansion coefficient β^{σ} for CO_2 (K^{-1})	3.3×10^{-3}
Thermal expansion coefficient β^{σ} for 2 M methanol–water solution (K^{-1})	3.3×10^{-4}
Gravitational constant **G** (cm s^{-2})	0.001

is fixed at 250 μm s^{-1} in this case and the bubble transport velocity is calculated to be 272.1 μm s^{-1}. If we define the bubble length as the distance between the front and the rear end of the bubble slug, the bubble length in this base case is 3.71 μm by measurement from the density plot. The temperature distribution of the flow field versus elapsed time, shown in Fig. 3(b), reveals that small temperature difference exists at the interface between the gas and the liquid phases. This temperature difference can be visualized since the Boltzmann equation is basically a non-continuum model. The TLBM scheme is possible to deal with the discontinuity problem in the two-phase flow. Uniform temperature distribution of the flow field indicates that heat quickly transfers from walls to the fluid. The temperature of the bubbly flow immediately reaches the same temperature as both walls (308 K).

Under the same flow conditions, we use the VOF method to simulate the same case. The size of each computational grid used in the VOF simulation is identical to that used in the TLBM simulation. Fig. 4(a) illustrates the CO_2 volume fraction at different elapsed time. Note that the CO_2 volume fraction in this figure represents the occupancy of the CO_2 in a computational grid which comprises the fluid domain. The red part means that the fluid domain is occupied by CO_2 bubbles while the purple part indicates the existence of the methanol–water solution in the fluid domain. It is clearly demonstrated that the shape of the CO_2 bubble shown in Fig. 4(a)
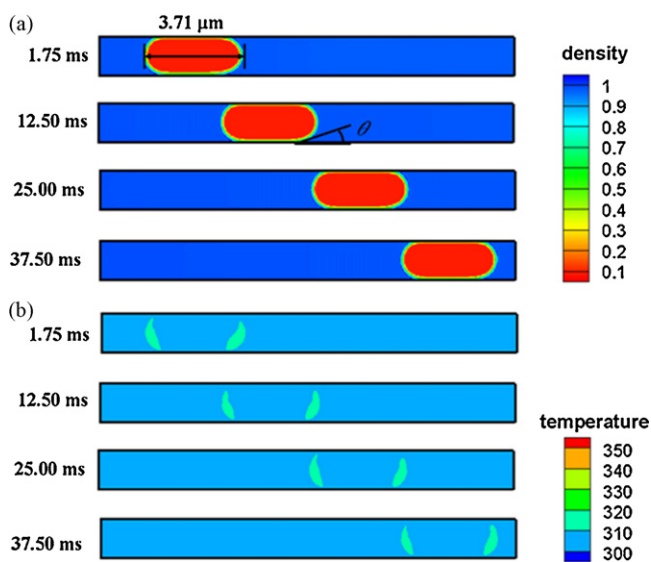

Fig. 3. TLBM simulation results: (a) density plots of the bubbly flow at different elapsed time. The length of the bubble is 3.71 μm and the contact angle θ is 18° in this baseline case (wall temperature: 308 K; inflow velocity: 250 μm s^{-1}); (b) corresponding temperature distribution of the bubbly flow.
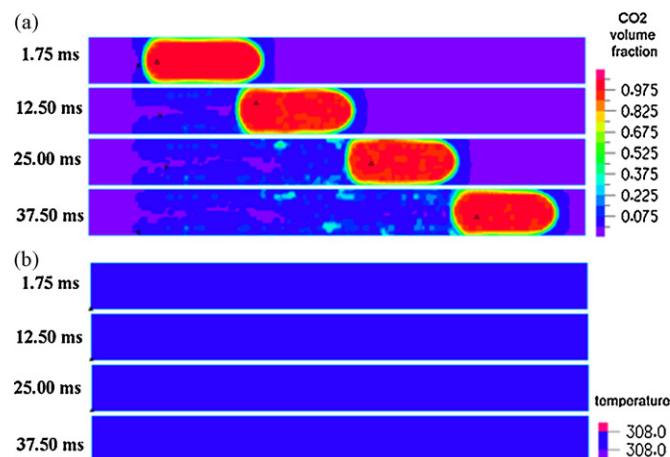

Fig. 4. VOF simulation results: (a) CO_2 volume fraction plot at different elapsed time. The red color means that the fluid domain is occupied by CO_2 while the purple part represents the methanol–water solution; (b) corresponding temperature distribution of the bubbly flow. (For interpretation of the references to color in this figure legend, the reader is referred to the web version of the article.)

is qualitatively identical to that shown in Fig. 3(a). The bubble is slug-like as it is constrained in the microchannel. The length of the bubble is also 3.71 μm and the bubble transport velocity is 272.0 μm s^{-1} in this case. There are some bubble residuals along the flow path; this is due to the numerical scheme to calculate the volume fraction. Fig. 4(b) shows that the temperature distribution of the bubbly flow in the microchannel under steady state is entirely uniform. Heat is evenly conducted from both upper and bottom walls to the two-phase flow and the temperature of the entire domain reaches 308 K. The temperature difference across the liquid and the bubble is continuous and it is zero under steady state using this continuum approach.

Velocity fields of the bubbly flow from both TLBM and VOF simulations are compared in Fig. 5. The enlarged diagrams of the velocity vector shows that the surface tension acting on the bubble surface is a cohesive force. Therefore, it can be observed from both Fig. 5(a) and (b) that the direction of the velocity vectors at the surface of the CO_2 bubble is inward to minimize the surface of the gaseous bubble. Inside the bubble slug, there are vortexes at both ends. Since the CO_2 bubble moves from left to right in this case, the velocity vectors at the central part of the bubble and at the methanol–water solution part are in the same moving direction.
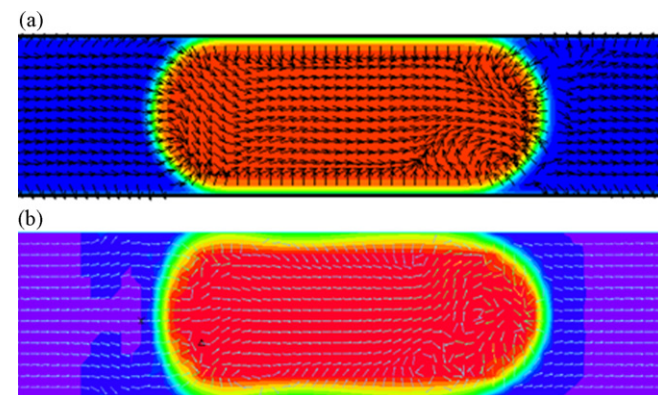

Fig. 5. Enlarged diagrams of the velocity vectors from (a) TLBM and (b) VOF simulations. The direction of the velocity vectors at the surface of the CO_2 bubble is inward which minimizes the surface of the gaseous bubble. Inside the bubble slug, there are vortexes at both ends. The velocity vectors at the central part of the bubble and at the methanol–water solution part are in the same moving direction.

Table 2
Input parameters for evaluating the surface tension at different temperature using the VOF and TLBM simulations.

Temperature (K)	VOF	TLBM
	Surface tension coefficients κ_{jk} ($\times 10^3$ N m^{-1})	Interaction strength between different species $G^{\sigma\sigma'}$ (cm^3 g^{-1} s^{-1})
298	55.16	3.80
303	54.62	3.79
308	54.06	3.78
313	53.29	3.77
318	52.66	3.76
323	52.01	3.74

3.2. Thermal effect on the bubble size

To investigate the thermal effect on the size of the CO_2 bubbles, several cases with constant wall temperature are imposed on both upper and bottom walls of the microchannel. The constant wall temperature ranges from 298 K to 323 K in a step of 5 K, which is approximately equal to the temperature range of the DMFC operation. Simulations are performed using both TLBM and VOF methods. Table 2 shows input parameters for evaluating the surface tension at each corresponding temperature.

Fig. 6 shows the relationship between the bubble length and the wall temperature. In this figure, red square symbols represent the TLBM and blue triangles for the VOF results. Both predictions show good agreement with each other. The bubble length decreases as the wall temperature increases. This is because when the temperature increases, the surface tension decreased (Table 2). The bubble volume supported by the surface tension is reduced, making the size of the bubble smaller. The length of the CO_2 bubble slug is thus decreased.

3.3. Thermal effect on the bubble transport velocity

Fig. 7 shows the CO_2 bubble transport velocity in the microchannel versus the wall temperature from both TLBM and VOF simulations. Again both predictions show good agreement with each other. As stated previously, the bubble size is smaller in the high-temperature solution than in the low-temperature. The variation of the bubble size influences the mobility of the bubble in the microchannel. When the bubble size decreases due to the rise of the temperature, the mobility of the bubble is thus increased. Therefore, the bubble transport velocity increases with the wall temperature; that means the bubble moves
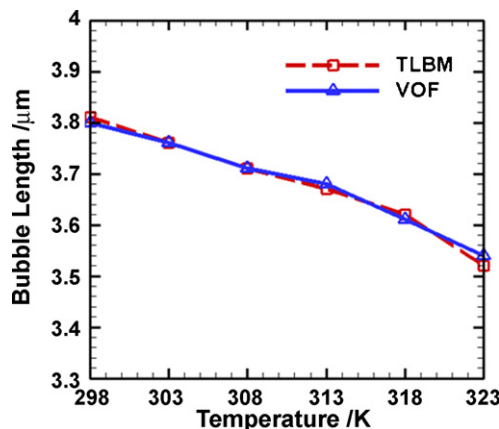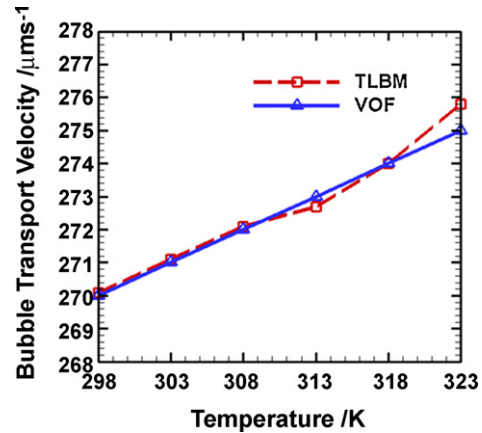

Fig. 7. Bubble transport velocities in the microchannel calculated from both TLBM and VOF simulations with different wall temperatures (inflow velocity: 250 μm s^{-1}).

faster in the high-temperature liquid than in low-temperature ones.

3.4. Marangoni effect

As mentioned earlier, the temperature gradient can be used as a driving force for the bubble movement in the microchannel. The bubble transport due to the temperature gradient is known as the Marangoni effect. To investigate this effect in detail, we perform the TLBM simulation with inlet flow velocity prescribed as zero, and with a constant wall temperature gradient from the inlet to the exit. Both upper and bottom wall temperatures vary from 298 K at the inlet to 333 K at the exit linearly, i.e. the temperature gradient ΔT is fixed at 35 K. Theoretically, when the inflow velocity equals to zero, the CO_2 bubble ought to be stationary in the horizontal microchannel. However, as shown in Figs. 8(a) and 9, the bubble gradually transports along the microchannel with the velocity of 50 μm s^{-1} when the inflow velocity is zero. It is proven that the imposed positive temperature gradient is responsible for the bubble transport in this case. The bubble transports automatically from the low-temperature (298 K) inlet to the high-temperature (333 K) exit of the microchannel. The contact angle increases from $\theta_1 \approx 20°$ to $\theta_2 \approx 30°$ then to $\theta_3 \approx 35°$ and finally to $\theta_4 \approx 40°$, as shown

Fig. 6. Bubble length versus wall temperature from both TLBM and VOF simulations; they show excellent agreement.
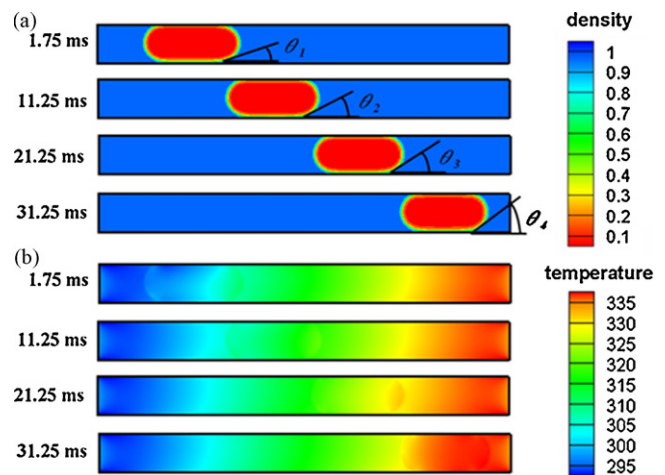

Fig. 8. (a) TLBM density plot of the bubbly flow at different elapsed time; the contact angle increases with the increasing wall temperature ($\theta_1 \approx 20° < \theta_2 \approx 30° < \theta_3 \approx 35° < \theta_4 \approx 40°$); (b) corresponding temperature distribution of the bubbly flow at each elapsed time; the wall temperature varies from 298 K at the inlet to 333 K at the exit.
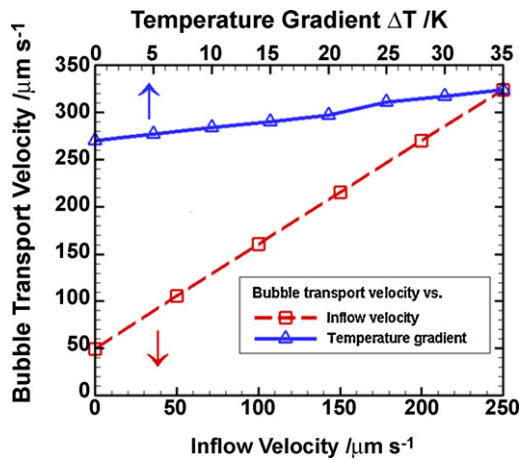
Fig. 9. Bubble transport velocities in the microchannel under different inflow velocities and wall temperature gradients. The relationship between the bubble transport velocity and the inflow velocity is shown by square symbols (temperature gradient is fixed at 35 K, from 298 K at the inlet to 333 K at the exit). Triangular symbols show the relationship between the bubble transport velocity and the temperature gradient (inflow velocity is fixed at 250 μm s^{-1}).

in Fig. 8(a). This is due to the increasing flow temperature from inlet to exit, as shown in the corresponding temperature field diagram in Fig. 8(b).

The effect of the imposed wall temperature gradient on the bubble transport velocity can be further observed by altering the imposed wall temperature gradient (inflow velocity kept at constant). The blue line in Fig. 9 indicates the relationship between the bubble transport velocity and the imposed wall temperature gradient. The inflow velocity of each case is set at 250 μm s^{-1} and the wall temperature at the inlet is 298 K. Only the wall temperature at the exit of the microchannel is changed from 298 to 333 K, meaning that ΔT varies from 0 to 35 K. Simulation results reveal that the bubble transports more rapidly in the microchannel when the wall temperature gradient is increased. The imposed positive wall temperature gradient is therefore favorable for the bubble transport in the microchannel. The CO_2 bubble can be removed from the microchannel if the temperature gradient technique is applied in the bubbly flow. The red line in Fig. 9 shows the relationship between the bubble velocity and the inflow velocity at fixed temperature gradient. As the inflow velocity increases, the bubble transport velocity increases correspondingly because of the increased momentum provided by the inflow micro-pump.

Note that Figs. 8 and 9 are not able to be verified by the VOF technique. This is because we can implement our self-written TLBM code with the relationship between the surface tension and the flow temperature in the scheme (as shown in Table 2); however, the VOF code is a commercial binary code that we are not able to add the function in Table 2 to correct its surface tension coefficient with respect to the varying flow temperature. Hence, the VOF scheme can only be applied to the constant wall temperature cases in this paper.

4. Conclusions

Thermal effects on the CO_2 bubble transport phenomena in an anodic microchannel of a DMFC have been analyzed qualitatively and quantitatively in this research. Both TLBM and VOF schemes have been employed to investigate the bubble dynamics. Simulation results show that the shape of the CO_2 bubble in the microchannel is constrained by the channel dimension and becomes a bubble slug. The bubble slug is pushed by the inflow methanol–water solution and gradually moves from the inlet to

the exit of the microchannel. The TLBM prediction of the bubble transport velocity is 272.1 μm s^{-1} and the bubble length is 3.71 μm when the inflow velocity is 250 μm s^{-1} and the wall temperature is fixed at 308 K. These quantitative data are verified by the VOF simulation on a commercial CFD package. Similar bubble transport phenomena are observed from the results of the TLBM and the VOF simulations. However, the TLBM reduces the computation time to the order of one tenth, but with the same accuracy as the VOF does. The computation times on the same simulation case at the same personal computer are approximately 1 h for TLBM and 10 h for VOF.

Thermal effects play an important role in the bubble dynamics since the surface tension between the CO_2 bubble and the methanol–water solution is temperature-dependent. Both TLBM and VOF simulation results indicate that the bubble size reduces when the wall temperature in increased. The variation of the bubble size evidently affects the mobility of the bubble transport in the microchannel. Small bubbles have higher mobility than the large bubble, meaning that small bubbles move faster in the microchannel with high wall temperature. The relationship between the bubble transport velocity and the wall temperature obtained from both simulation techniques show good agreement. The bubble is able to move automatically in the horizontal microchannel even under the condition of zero inflow velocity with a temperature gradient imposed along the channel. The bubble transport velocity increases when the imposed temperature gradient is increased.

In summary, the TLBM scheme developed in this work has been proven to be an effective simulation tool to analyze the CO_2 bubble transport phenomena in the DMFC microchannel, especially under the varying temperature cases. The simulation results presented in this paper are helpful and valuable to the research and development of the bubble removal technique for DMFCs. The self-written TLBM scheme has been proven to be an effective and extremely fast numerical technique to simulate the bubbly thermal flow in the DMFC microchannel.

Acknowledgements

References

[1] G.O. Lu, C.Y. Wang, J. Power Sources 134 (2004) 33–40.
[2] H. Yang, T.S. Zhao, Q. Ye, J. Power Sources 139 (2005) 79–90.
[3] C.W. Wong, T.S. Zhao, Q. Ye, J.G. Liu, J. Electrochem. Soc. 152 (2005) A1600–A1605.
[4] K. Fei, C.H. Cheng, C.W. Hong, J. Fuel Cell Sci. Technol. 3 (2006) 180–187.
[5] K. Fei, C.W. Hong, Microfluid Nanofluid 3 (2007) 77–88.
[6] N.O. Young, J.S. Goldstein, M.J. Block, J. Fluid Mech. 6 (1959) 350–356.
[7] T.K. Jun, C.J. Kim, J. Appl. Phys. 83 (1998) 5658–5664.
[8] K. Takahashi, J.G. Weng, C.L. Tien, Microscale Therm. Eng. 3 (1999) 169–182.
[9] K. Takahashi, K. Yoshino, S. Hatano, K. Nagayama, T. Asano, Proceedings of the IEEE Micro Electro Mechanical Systems (MEMS), 2001, pp. 286–298.
[10] X. Shan, Phys. Rev. E 55 (1997) 2780–2788.
[11] Y. Shi, T.S. Zhao, Z.L. Guo, Phys. Rev. E 70 (2004), 066310-1–066310-10.
[12] Z. Guo, C. Zheng, B. Shi, T.S. Zhao, Phys. Rev. E 75 (2007), 036704-1–036704-15.
[13] K. Fei, W.H. Chen, C.W. Hong, Microfluid Nanofluid 5 (2008) 119–129.
[14] D. Lörstad, L. Fuchs, J. Comput. Phys. 200 (2004) 153–176.
[15] T. Taha, Z.F. Cui, Chem. Eng. Sci. 61 (2006) 676–687.
[16] X. Zhu, P.C. Sui, N. Djilali, Microfluid Nanofluid 4 (2008) 543–555.
[17] C.W. Hirt, B.D. Nichols, J. Comput. Phys. 39 (1981) 201–225.
[18] K.J. Bathe, Theory and Modeling Guide Volume III: ADINA CFD & FSI, ADINA R&D, Inc., 2005.
[19] D.L. Youngs, in: K.W. Morton, M.J. Baibnes (Eds.), Numerical Methods for Fluid Dynamics, Academic Press, New York, 1982.
[20] J.U. Brackbill, D.B. Kothe, C. Zemach, J. Comput. Phys. 100 (1992) 335–354.